Rift-inversion orogens are potential hotspots for natural H2 generation

Frank Zwaan

frank.zwaan@gfz-potsdam.de

GFZ German Research Centre for Geosciences https://orcid.org/0000-0001-8226-2132

Sascha Brune

German Research Centre for Geosciences GFZ & University of Potsdam https://orcid.org/0000-0003-4985-1810

Anne Glerum

https://orcid.org/0000-0002-9481-1749

Dylan A. Vasey

Tufts University https://orcid.org/0000-0002-2182-4733

John B. Naliboff

New Mexico Institute of Mining and Technology https://orcid.org/0000-0002-5697-7203

Gianreto Manatschal

IPGS - EOST - Université de Strasbourg https://orcid.org/0000-0003-3834-2033

Eric C. Gaucher

Lavoisier H2 Geoconsult https://orcid.org/0000-0002-7976-8455

Article

Keywords:

Posted Date: October 17th, 2023

DOI: https://doi.org/10.21203/rs.3.rs-3367317/v1

Additional Declarations: There is **NO** Competing Interest.

Rift-inversion orogens are potential hotspots for natural H_2 generation

Frank Zwaan[1,2*], Sascha Brune[1,3], Anne Glerum[1], Dylan A. Vasey[4], John B. Naliboff[5], Gianreto Manatschal[6], Eric C. Gaucher[7]

[1]GFZ German Research Centre for Geosciences, Telegrafenberg, 14473 Potsdam, Germany

[2]University of Fribourg, 1700 Fribourg, Switzerland

[3]Institute of Geosciences, University of Potsdam, Potsdam, Germany

[4]Department of Earth and Climate Sciences, Tufts University, Medford, MA 02155, USA

[5]Department of Earth and Environmental Science, New Mexico Institute of Mining and Technology, Socorro, NM 87801, USA

[6]University of Strasbourg, CNRS, ENGEES, ITES UMR 7063, Strasbourg, France

[7]Lavoisier H_2 Geoconsult, 74400 Chamonix, France

Contact: frank.zwaan@gfz-potsdam.de

***Word count** (excluding Abstract, figure captions, Acknowledgements, and Methods): 2673*

***Figure count** (excluding Methods): 6*

ABSTRACT

Naturally occurring hydrogen gas (H_2) represents a potentially major source of clean energy. The most promising mechanism for large-scale natural H_2 generation is serpentinization where mantle material reacts with water while passing through a temperature-dependent "serpentinization window" (T = 200-350˚C) during mantle exhumation. We study such serpentinization-related natural H_2 generation during rifting and subsequent formation of rift-inversion orogens by means of numerical geodynamic models. In these models we trace how, when, and where mantle material enters the serpentinization window, as well as when active deformation along fault zones in mantle bodies may allow for water circulation and serpentinization to occur. Although serpentinization-related natural H_2 generation is best known from rifted margins and spreading ridges, we find that volumes of natural H_2 generated during inversion may be up to 20 times larger than during rifting, due to a colder thermal regime. Moreover, suitable reservoirs and seals are readily available in rift-inversion orogens, whereas they may not be present during serpentinization in rift settings. Our model results thus provide a first-order motivation to turn to rift-inversion orogens for natural H_2 exploration, as supported by indications of natural H_2 generation in the Western Alps, Pyrenees, and Caucasus.

A key challenge for the 21st century is the development of sustainable energy sources. Molecular hydrogen gas (henceforth "H_2") may be one of our best alternatives to hydrocarbon-based fuels, but present-day synthetic H_2 production is still very expensive (39; 16). However, H_2 is also generated by a range of natural (bio)chemical processes in the lithosphere (e.g., 43). This natural H_2 may represent an excellent source of sustainable energy that, until recently, has been mostly overlooked (e.g., 35; 13).

The most promising mechanism for large-scale natural H_2 generation is water-induced alteration (serpentinization) of mantle rocks (35; 20). Dense mantle rocks are usually located deep in the Earth and need to be exhumed (here defined as being brought above the original base of the crust [Moho] by tectonic and erosional processes) to undergo serpentinization. This reaction requires circulation of water in a liquid state and is most efficient at temperatures between ca. 200 to 350°C, within the "serpentinization window" (7). Such mantle exhumation and associated natural H_2 generation through serpentinization is well-documented along rifted margins and mid-ocean ridges (1; 23). Mantle exhumation is also known from rift-inversion orogens formed during the Wilson cycle (42) and associated large-scale inversion of rift basins (e.g., in the Alpine-Tethyan collisional belt, Fig. 1). Moreover, indications of natural H_2 generation from serpentinized mantle occur in the French Pyrenees (21; 22). Elevated natural H_2 concentrations are also reported in the Western Alps (6; 15), and a Soviet-era well in the Caucasus produced natural H_2 for several months (43).

Our understanding of the dynamics and timing of mantle exhumation and serpentinization processes in rift-inversion orogens, crucial to assess the associated natural H_2 potential (39), remains restricted so far, especially since these processes occur at great depth. Here, numerical geodynamic modelling provides a means to gain key insights, and various researchers have numerically modelled rift-inversion orogens (e.g., 17; 18; 8; 9; 31; 19; 14; 40). Still, these studies

mostly focused on the overall crustal structure of rift-inversion orogen, whereas only limited and qualitative attention was dedicated to the exhumation (and serpentinization) of mantle material.

In this paper we use the thermo-mechanical geodynamic code ASPECT coupled with the surface processes code FastScape to conduct numerical models of rift-inversion orogens (Figs. 2-5, see also the Methods). In our models, we systematically quantify the impact of initial rifting duration and the length of the post-rift cooling phase on mantle exhumation in rift-inversion orogens, which lead to three end-member orogenic styles (Figs. 2-5, and Supplementary Material) (45). We subsequently assess the associated serpentinization and natural H_2 potential, and propose that rift-inversion orogens, rather than rifts or rifted margins, may provide the best targets for natural H_2 exploration (Fig. 6).

RESULTS

Our models can be described in terms of three end-member styles (Style I: symmetric, Style II: asymmetric, and Style III: symmetric, with a large core of exhumed mantle material) (Fig. 3). Throughout each model's tectonic evolution, we quantify, in 2D section view: (I) the area of exhumed mantle (i.e. the area of mantle material found above the pre-rift Moho, which is at 35 km depth in our models), (II) the area of actively exhuming mantle (i.e. exhumed mantle that is moving upward), and (III) the serpentinization window size, (i.e., the area of exhumed mantle material with temperatures between 200˚ and 350˚C), which allows for geologically instantaneous serpentinization (e.g., 7) (Fig. 2). Subsequently, we compute (IV) serpentinization capacity, (V) cumulative serpentinization, (VI) natural H_2 capacity, and (VII) cumulative natural H2 generation over time (Fig. 4) following the methodology from Liu et al. (2023) (23). This method accounts for the presence of active fault zones acting as pathways for water circulation needed for

serpentinization of mantle rocks in the serpentinization window (3). See the Methods for more details, and the Supplementary Material (45) for all model results produced for this study.

Rift-inversion orogen style I (M1)

End-member model M1 represents the symmetric orogenic Style I, typical of systems with short rift durations (Figs. 3a-e, 4a, d). During the initial 5 Myr of rifting a symmetric fault-bounded basin forms as lithosphere starts to thin locally (Fig. 3a). Once rifting ends, 30 Myr of shortening ensues without a post-rift cooling interval (Fig. 3c-e). The rift basin is inverted within 5 Myr, and a largely symmetric orogen consisting of crustal material with a small core of mantle material develops (Figs. 3c-e). The short rifting phase in M1 allows for a very limited (linear) increase in exhumed mantle area (until a maximum of $\sim 1 \cdot 10^9$ m^2), but almost all mantle material is buried again during subsequent inversion (Figs. 3c-e, 4a). Consequently, a very limited serpentinization window develops, the serpentinization capacity per along-strike unit length remains below $1 \cdot 10^8$ kg(yr·km)$^{-1}$, and total serpentinization and natural H_2 generation are negligible (Fig. 4d).

Rift-inversion orogen style II (M5)

Asymmetric orogenic Style II, typical of systems with longer rift durations but limited post-rift cooling prior to inversion, is represented by model M5 (Figs. 3f-j, 4b, e). Here we apply 15 Myr of extension so that at the end of rifting mantle is exhumed near the surface with only a sparse (1-4 km) cover of crustal material and sediments (Figs. 3f). Mantle exhumation over time follows a similar initial increase as seen in M1 but is much more significant in M5 ($\sim 3.5 \cdot 10^9$ m^2 at the end of rifting, Fig. 4b). The actively exhuming mantle area shows deviation from the total exhumed mantle trend after 8 Myr (Fig. 4b). The exhumed mantle area remains stable during the subsequent 20 Myr of post-rift cooling, apart from a slow gradual decline due to thermal sag and sediment accumulation (Fig. 4b). However, a significant part of the mantle material continues to rise during

cooling, due to isostatic balancing of rift shoulder erosion (Fig. 4b). During inversion, most exhumed mantle is buried again, but the formation of an asymmetric orogen causes a block of (lithospheric) mantle to be thrust on top of the downgoing plate (shown by the exhuming mantle area during inversion), keeping mantle material near the surface (Figs. 3g-h, 4b).

Exhuming more mantle rocks in model M5 means a significant amount of mantle material is found in the serpentinization window by the end of rifting, and this amount further increases during post-rift cooling (Figs. 3f, g, 4b). Consequently, serpentinization and natural H_2 generation capacities at the end of rifting are much higher than in M1 (i.e., about $5 \cdot 10^9$ kg/(yr·km) and $1.5 \cdot 10^8$ mol/(yr·km), respectively) but drop to zero during post-rift cooling as no further strain localizes in the serpentinization window (Fig. 3g, 4e). The subsequent overthrusting of mantle material within a relatively cool orogen focuses strain along mantle fault zones within the serpentinization window again, and on a much larger scale (Fig. 3h-j). From the start of inversion, serpentinization and natural H_2 generation capacity thus hover around ~$1 \cdot 10^{11}$ kg/(yr·km) and $3 \cdot 10^8$ mol/(yr·km), about 20 times higher than at the end of rifting, as also highlighted by the considerable increase in cumulative serpentinization during inversion (Figs. 4e). The notable drop in serpentinization capacity at ~50 Myr indicates a temporary migration of strain away from the serpentinization window (Fig. 4e).

Rift-inversion orogen style III (M9)

Model M9 represents symmetric orogenic Style III, typical of systems with both long rift durations and prolonged post-rift cooling prior to inversion (Figs. 3k-o, 4c, f). In this model, 25 Myr of rifting leads to a linearly increasing exhumed mantle area (up to ca $7 \cdot 10^9$ m^2 at the end of rifting), with only 1-4 kms of sediment remaining on the exhumed mantle (whereas no oceanic crust is generated, Figs. 3k, 4c). Similar to M5, the area of actively exhuming mantle deviates from the

133 total exhumed mantle area after 8 Myr of rifting (Fig. 4c). Post-rift cooling also causes a gradual
134 decline in exhumed mantle area before most mantle material is brought down again during
135 inversion (Figs. 3m-o, 4c). Yet, in contrast to M5, the cooling of the extensive amount of exhumed
136 mantle material causes a fault zone to develop near the basin centre, so that a large block of mantle
137 is preserved in a roughly symmetric orogen (Fig. 3m-o). Although most mantle material is buried
138 again, there is actively exhuming mantle during both post-rift cooling and subsequent inversion
139 (Fig. 4c).
140
141 The cooling of a larger exhumed mantle area over a longer time span in M9 also means that more
142 mantle material is found in the serpentinization window than in M5 (Figs. 3g, l, 4b, c). However,
143 the maximum serpentinization capacity of ~$5 \cdot 10^{9}$ kg(yr·km)$^{-1}$ and the natural H_2 generation
144 capacity of $1.5 \cdot 10^{8}$ mol(yr·km)$^{-1}$ during rifting are similar in both M5 and M9, suggesting an upper
145 limit imposed by the vertical extent of the serpentinization window (Fig. 4e, f). As in M5, post-rift
146 tectonic quiescence halts serpentinization, which renews during inversion, and the strong increase
147 in total serpentinization since the start of inversion is linked to relatively constant serpentinization
148 and natural H_2 generation capacities of ~$1 \cdot 10^{11}$ kg(yr·km)$^{-1}$ and $3 \cdot 10^{10}$ mol(yr·km)$^{-1}$, respectively
149 (Figs. 3g, l, 4e, f). These values, found in both models (and in other models with sufficient initial
150 rifting [Styles II and III]) (see Supplementary Material, [45]), indicate serpentinization and H_2
151 generation rates during inversion that are 20 times higher than these rates observed during rifting
152 (Figs. 4e, f, 5).
153
154 **4. DISCUSSION**
155 **General mantle exhumation patterns**
156 Our numerical models provide insight into the factors enabling exhumation and preservation of
157 mantle material in rift-inversion orogens (Figs. 3-5). The first key requirement is for rifting to

158 exhume sufficient mantle material above the pre-rift Moho depth in the first place. Although the
159 bulk of this material is forced back down again by subsequent inversion, some exhumed mantle
160 may be preserved or further exhumed in the orogen (especially in asymmetric orogens, i.e. Style
161 II or III) (Figs. 3-5), as qualitatively observed in previous modelling studies (17; 8; 18, 31; 19; 40).
162
163 **Natural H_2 potential in rift-inversion orogens**
164 After sufficient extension, a large volume of mantle can be exhumed during rifting (Figs. 2-5). As
165 rift settings are marked by high temperatures at shallow depth, only a small part of this exhumed
166 mantle material enters into the temperature-defined serpentinization window. Therefore, our
167 model serpentinization capacity during rifting is relatively low (i.e., around $5 \cdot 10^9$ kg(yr·km)$^{-1}$),
168 which is very similar to values calculated for North Atlantic rifting (23). By contrast, the
169 serpentinization capacity during inversion is about 20 times higher (~$1 \cdot 10^{11}$ kg(yr·km)$^{-1}$), due to
170 the combination of a much larger serpentinization window in a orogen with relatively low thermal
171 gradients and larger fault zones cutting the mantle that enable the efficient water circulation needed
172 for serpentinization (3) (Figs. 3, 4). The bulk of serpentinization can thus be expected to take place
173 during inversion (Fig. 5). Still, if no active deformation occurs, no water would circulate and the
174 serpentinization capacity would drop, as highlighted by the lack of serpentinization during post-
175 rift quiescence (Figs. 3g, l, 4e-f). This need for localized deformation for mantle rocks to
176 serpentinize (3) also explains the occurrence of relatively fresh mantle material outcropping in
177 orogens such as the Pyrenees (e.g., 30; 37).
178
179 The serpentinization capacity in our models is directly translatable to potential natural H_2
180 generation capacity, which is ~$1.5 \cdot 10^8$ mol(yr·km)$^{-1}$ during advanced rifting and 20 times higher
181 (~$3 \cdot 10^{10}$ mol(yr·km)$^{-1}$) during inversion, indicating that the bulk of natural H_2 generation should
182 occur during inversion of rifts and rifted margins. Furthermore, the resulting rift-inversion orogens

generally contain large sediment volumes that can act as reservoirs and seals when natural H_2 is generated, in contrast to the likely absence of reservoir quality sediments at the time of bulk H_2 generation in the deep or distal environments of rifts and rifted margins (Figs 2-5). These reservoirs and seals are crucial for capturing natural H_2 migrating from the serpentinizing mantle and would enable the establishment of a fully-fledged "hydrogen system" (analogous to "petroleum systems", which involve a source rock generating the hydrocarbons and migration to reservoirs with a structure and cap rock where the hydrocarbons can accumulate so that they can be drilled and extracted) (22) (Fig. 6). Ideally natural H_2 fields should have reservoir temperatures between 100-200˚C, when H_2 is not consumed by microbial activity (38; 25; 22). Alternatively, the serpentinizing mantle rocks themselves could be targeted directly (Fig. 6). Our findings suggest that rift-inversion orogens provide much better environments for hydrogen exploration than rift or rifted margin settings.

Promising natural H_2 exploration sites in the Alpine-Tethyan domain

Overall, our models suggest that exploration for natural H_2 should focus on rift-inversion orogens, for example those found in the Alpine-Tethyan domain (Fig. 1). We clearly show that Style I orogens such as the Atlas are of low interest; they experienced limited rifting prior to inversion so that mantle rocks were not exhumed in the first place (2) (Fig. 1b).

More promising are orogens such as the Pyrenees, which show a gradient in initial rift basin maturity from limited rifting in the east to break-up and seafloor spreading in the Gulf of Biscay to the west (27; 11) (Fig. 1d-f). In the eastern Pyrenees, no evidence for present-day exhumed mantle has been reported (Style I) (27; 11) (Fig. 1f) but a shallow mantle body in a Style II setting is situated below the Mauléon Basin to the west (41) (Fig. 1e), where (21; 22) found evidence of on-going natural H_2 generation (Fig. 1d). Farther westward still, in the Bay of Biscay, mantle

material has not yet been incorporated and exhumed in the orogen, but this Style III setting could allow for migration of natural H_2 from the mantle to reservoirs on the basin margins.

The wider Alpine-Tethyan domain contains various rift-inversion orogens that formed after the closure of a number of small oceanic basins (e.g., 32; 33, 29) (Fig. 1a, g, h). For instance, seismic sections crossing the Western Alps show the presence of exhumed mantle in the retro-wedge, making the Italian flanks of the orogen a promising target for natural H_2 exploration in an asymmetric Style II setting (Figs. 1g, 3h-j). In fact, Dumagin et al. 2019 (6) found elevated concentrations of natural H_2 in the soil of the Western Alps. The highly-asymmetric (Western) Caucasus orogen also formed following closure of a rift that was possibly floored by oceanic crust (4; 5; 26) (Fig. 1c), and although no present-day exhumed mantle material has yet been reported, H_2 release has been documented in a Soviet-era well (43). The Betics, Dinarids, and Balkan area in general contain various ophiolites including exhumed mantle bodies that are linked to abiotic gas generation and warrant further exploration (32; 24) (Fig. 1a, f). The branches of the wider Alpine-Himalayan orogenic belt stretching farther eastward into Asia could also be of significant interest (12). The key challenge to natural H_2 explorers is to untangle the complex geologic history of these rift-inversion orogens (e.g., 32, 29).

CONCLUSION

Our numerical models provide quantified insights into mantle exhumation in rift-inversion orogens and into the associated natural H_2 potential. We find that:

- Initial rifting exhumes mantle material, the bulk of which is forced back down again by subsequent inversion. Yet some material may be incorporated in into the rift-inversion orogen.

- During rifting, the total volume of exhumed mantle increases linearly over time. However, due to high temperatures in combination with the limited scale of fault zones in the mantle, serpentinization capacity is relatively low, so that natural H_2 generation remains limited in rift or rifted margin settings. Moreover, the deep marine environment is not favourable to natural H_2 preservation due to a lack of suitable reservoirs during bulk natural H_2 generation.
- During inversion, natural H_2 generation capacity can be up to 20 times higher than during rifting since the serpentinization window is larger in a colder orogenic environment. Rift-inversion orogens are also much more likely to provide suitable reservoirs at the moment of bulk natural H_2 generation than rifts or rifted margin settings.
- A key requirement is that brittle deformation localizes within the serpentinization window, so that water circulation and thus serpentinization can occur.
- Our model results provide a first-order motivation to turn to rift-inversion orogens such as the Pyrenees, the Alps, the Betics, and the Caucasus for natural H_2 exploration.

ACKNOWLEDGMENTS

We thank our colleagues at the GFZ German Research Centre for Geosciences in Potsdam for valuable support and discussion. This research was funded via a GFZ Discovery Fellowship awarded to FZ. We gratefully acknowledge the computing time granted by the Resource Allocation Board and provided on the supercomputer Lise and Emmy at NHR@ZIB and NHR@Göttingen as part of the NHR infrastructure. The calculations for this research were conducted with computing resources under the project bbp00039.

FIGURES – MAIN TEXT

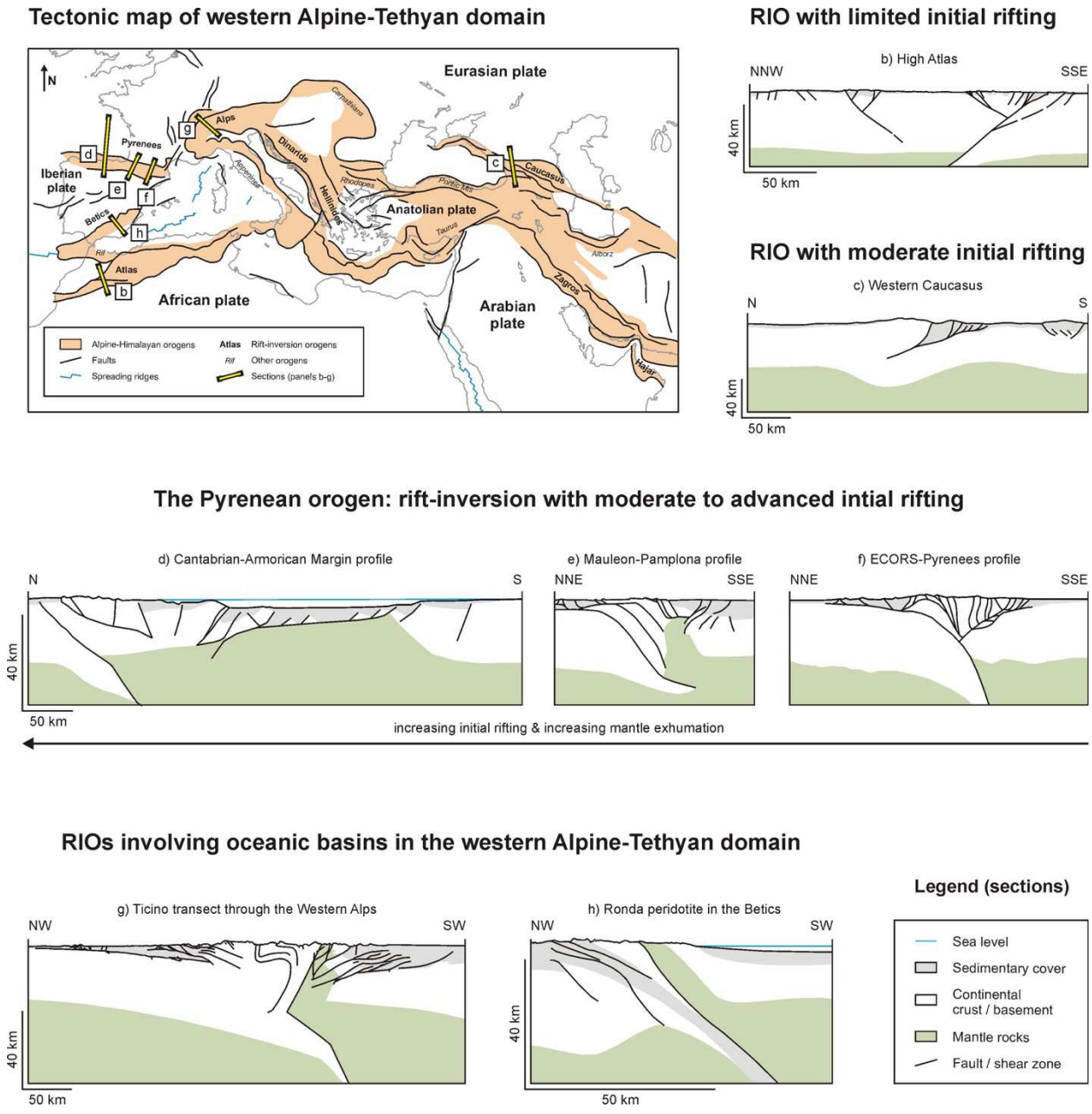

Figure 1. *Examples of rift-inversion orogens (RIOs) in the Alpine-Tethyan domain of the Alpine-Himalayan orogenic system. (a) Tectonic map of the Alpine-Tethyan domain, showing the locations of the sections in (b-h). Modified after Woudloper (Wikimedia) and (10). (b) High Atlas, a RIO with limited initial rifting and no exhumed mantle. Modified after (2). (c) Western Caucasus, a RIO with moderate initial rifting, but no present-day exhumed mantle. Modified after (28). (d-f) The influence of varying initial rifting duration along the Pyrenean system (increasing to the west), showing a general westward increase of present-day exhumed mantle. Modified after (27; 11). (g-h) Inversion of fully oceanic basins in the Alpine-Tethyan domain. Modified after (33;24).*

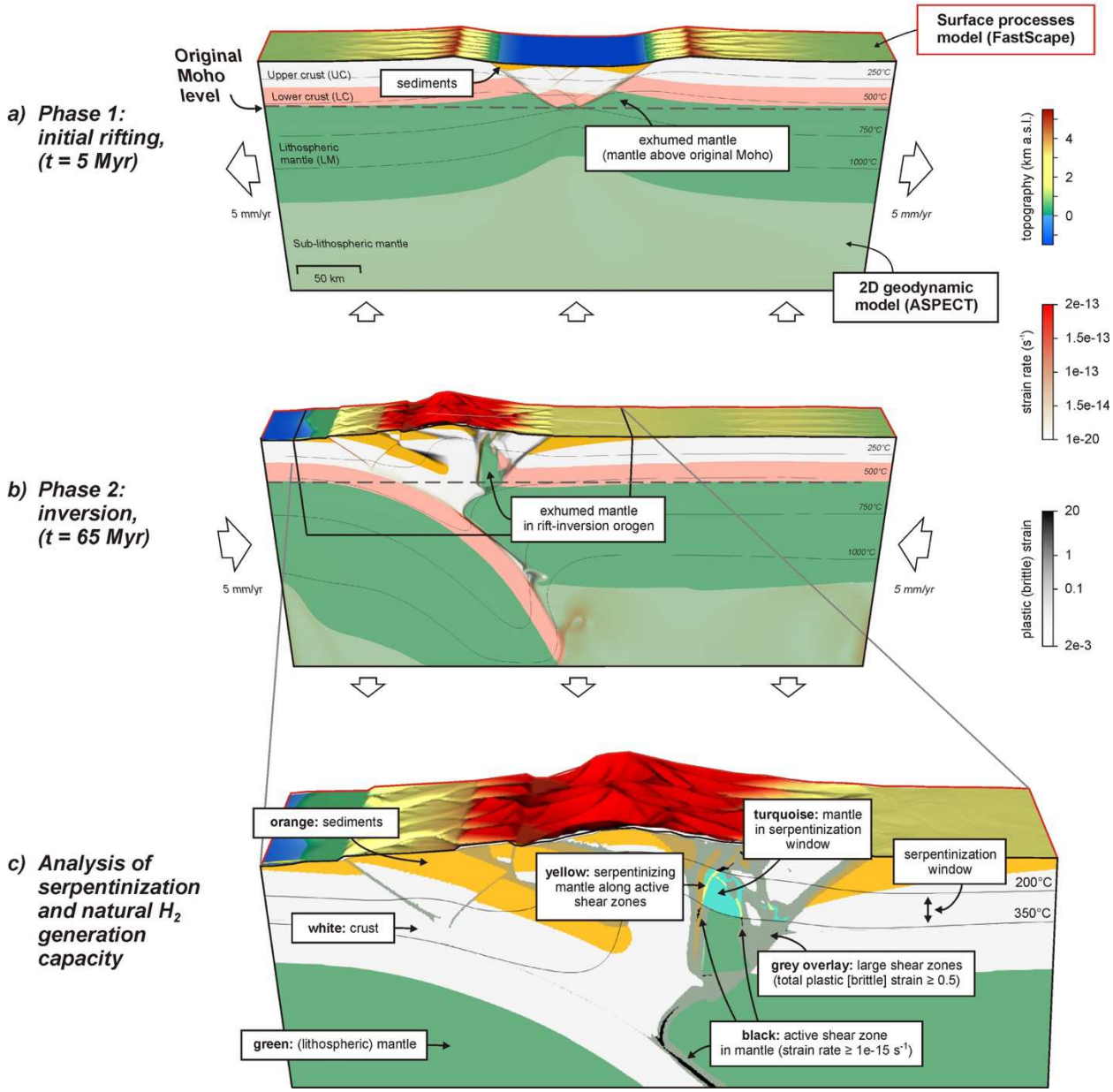

Figure 2. *Example of a model run. 3D rendering of model M5, with 15 Myr of initial rifting, followed by 20 Myr of tectonic pause before 30 Myr of inversion (a-b) General model evolution, with the definition of exhumed mantle (mantle material found above the initial base of the crust, i.e., above the original Moho). (a) Model state after 5 Myr of rifting. (b) Model state at the end of the model run (t = 65 Myr). (c) Definitions used for serpentinization and natural H_2 generation analysis. The ASPECT geodynamic model is 2D, whereas the FastScape surface processes model, acting on the upper limit of the ASPECT model, provides a quasi-3D model result. See Methods for more details.*

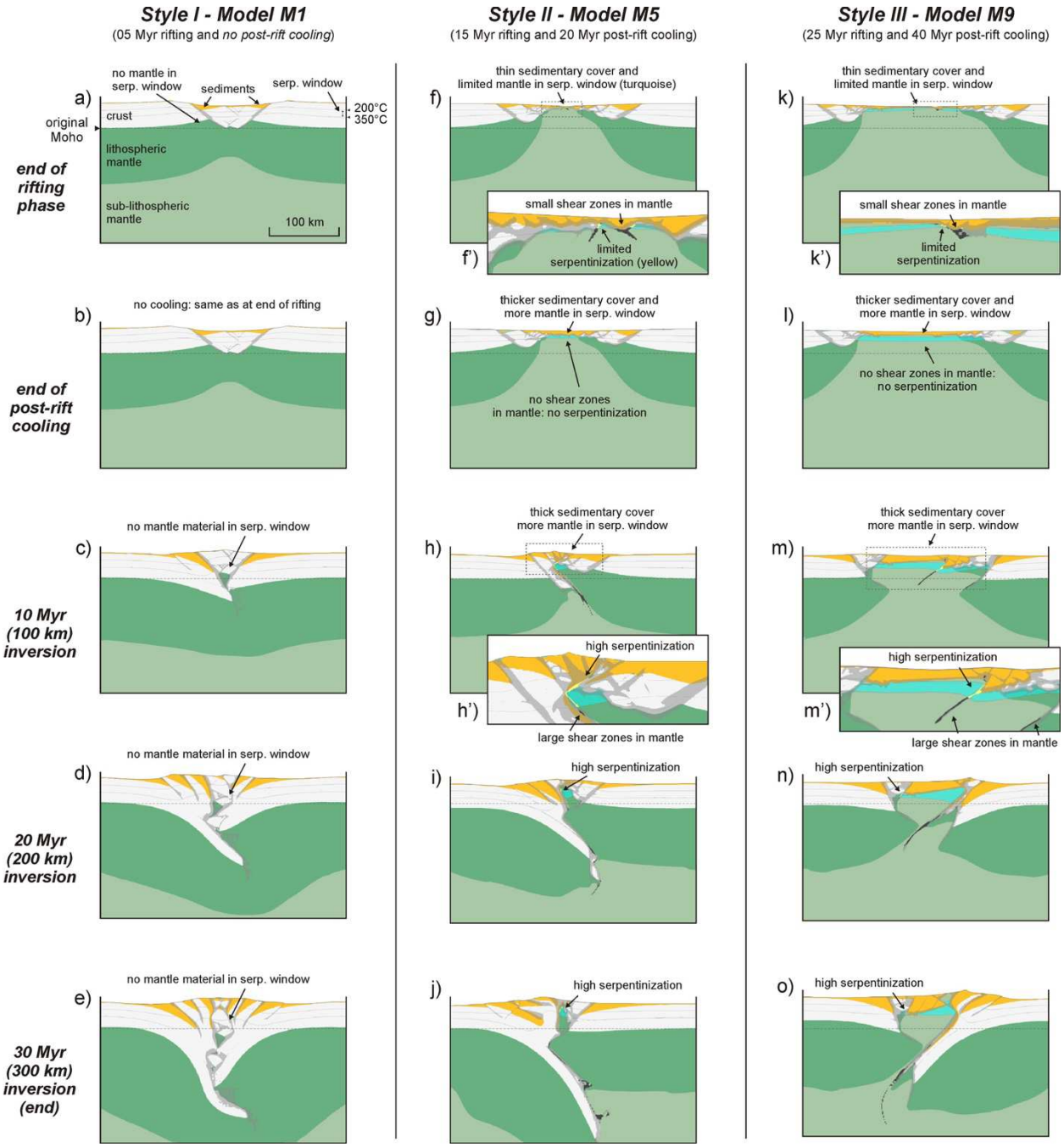

Figure 3. *Evolution of end-member rift-inversion orogen styles (from models M1, M5 and M9, representing styles I, II and III, respectively) and associated serpentinization. Insets (f', k', h', m') are used to highlight important details. Light green: sub-lithospheric mantle, dark green: lithospheric mantle, white: crust, orange: sediments, turquoise: mantle material in serpentinization window (between 200˚C and 350˚C isotherms), transparent grey: fault zones, black: active fault zones in mantle, yellow: active serpentinization. See also panels (a), (f) and (f'), and Fig. 2c. Limited serpentinization: up to* $5 \cdot 10^{9}$ *kg(yr·km)*$^{-1}$ *(during rifting), high serpentinization: up to* $1 \cdot 10^{11}$ *kg(yr·km)*$^{-1}$ *(during inversion). The results from the serpentinization and* H_2 *potential analysis are presented in Fig. 4.*

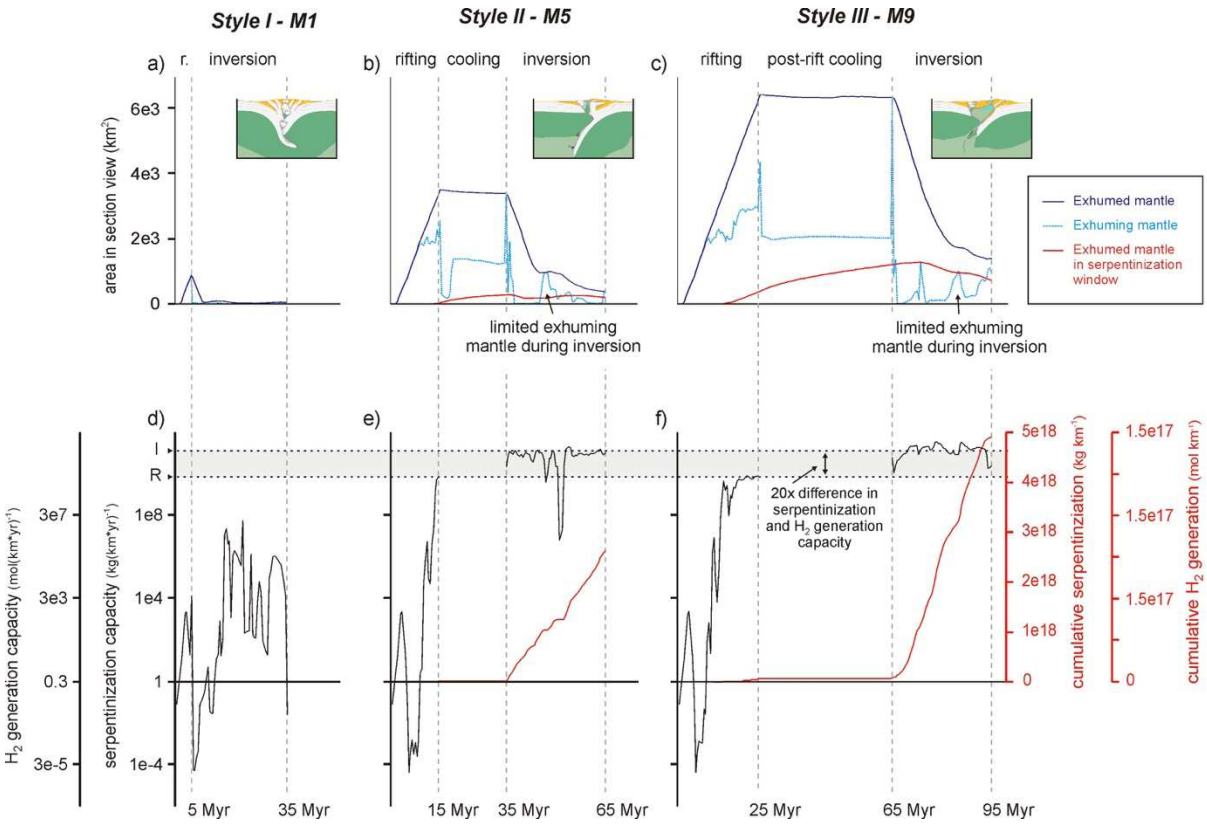

284

285

286 ***Figure 4.*** *Serpentinization and natural H_2 generation potential during the evolution of end-member rift-inversion orogen*
287 *styles (from models M1, M5 and M9, representing styles I, II and III, respectively, see also Fig. 3). (a-c) Total amount of*
288 *exhumed mantle (black), amount of actively exhuming mantle, i.e., upward vertical motion > 0 (turquoise), and mantle area*
289 *within serpentinization window over time (red) for each model. (d-f) Serpentinization capacity, natural H_2 generation*
290 *capacity (black), cumulative serpentinization, and cumulative natural H_2 generated over time (red). Due to the 2D modelling*
291 *geometry all values are provided per along-strike unit length. Assumption: 1 kg of serpentinized mantle material is assumed*
292 *to have generated 300 mmol of natural H_2 [1]). R and I: maximum serpentinization and natural H_2 capacity during rifting*
293 *and inversion, respectively (i.e., $0.5 \cdot 10^9$ and $1 \cdot 10^{11}$ kg(yr·km)$^{-1}$, and $1.5 \cdot 10^8$ and $3 \cdot 10^8$ mol(yr·km)$^{-1}$, respectively).*

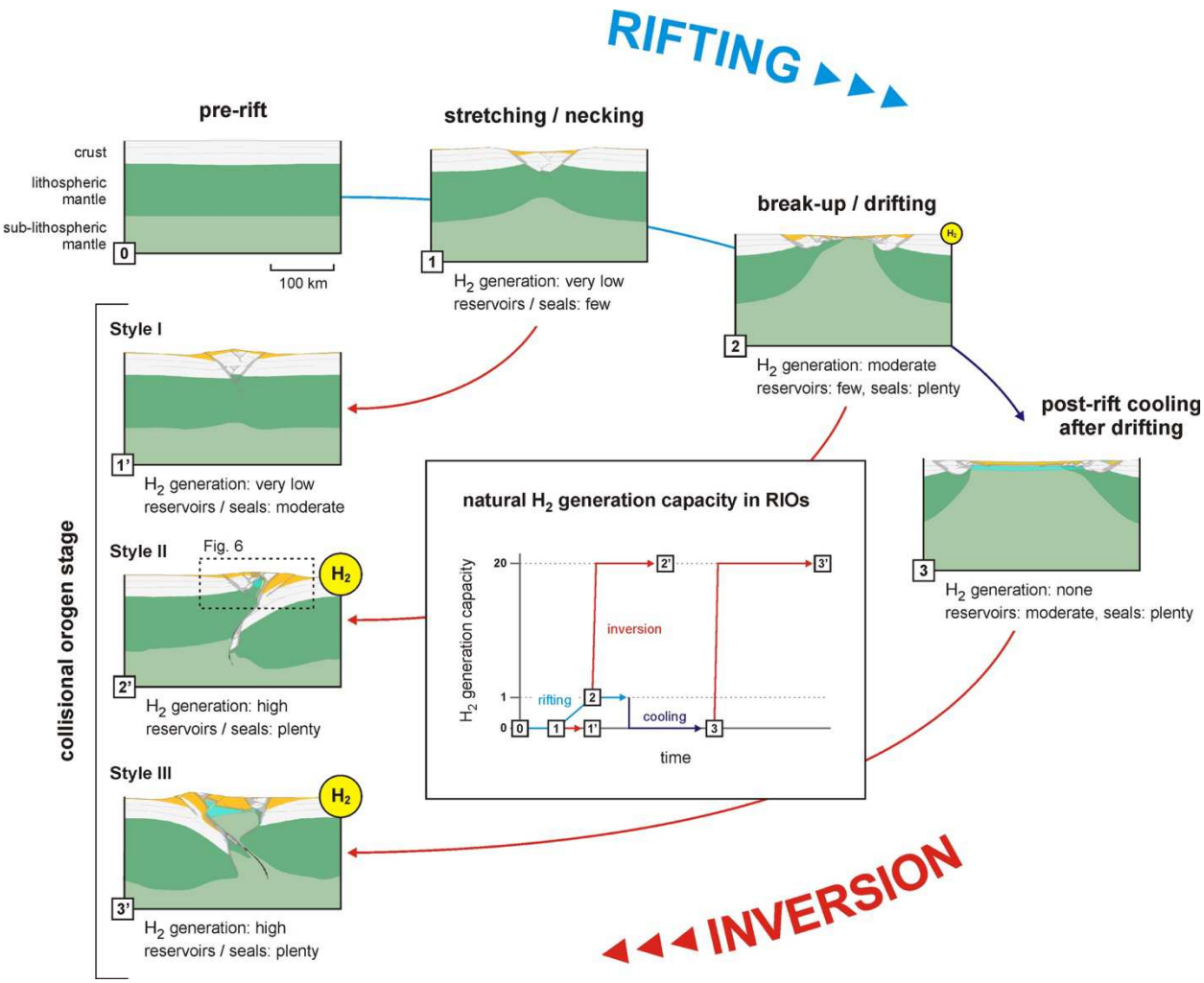

294

295

296 ***Fig. 5.*** *(a) Schematic summary of the evolution of natural H_2 potential during rifting and subsequent inversion. Depending*
297 *on rift duration and post-rift cooling, three rift-inversion orogen (RIO) styles can develop. Natural H_2 capacity (H_2*
298 *generation per time unit, as indicated by the yellow bubbles in the sections, as well as in the central graph) occurs in the*
299 *more advanced rifting stages, but is up to 20 times higher during inversion. However, faulting and associated water*
300 *circulation is required for natural H_2 generation, as highlighted by the absence of natural H_2 generation during post-rift*
301 *cooling. Light green: sub-lithospheric mantle, dark green: lithospheric mantle, white: crust, orange: sediments, turquoise:*
302 *mantle material in serpentinization window (between 200˚C and 350˚C isotherms), transparent grey: fault zones, black:*
303 *active fault zones in mantle, yellow: active serpentinization. See also See also Figs. 2c and 3a, f, f'.*

304

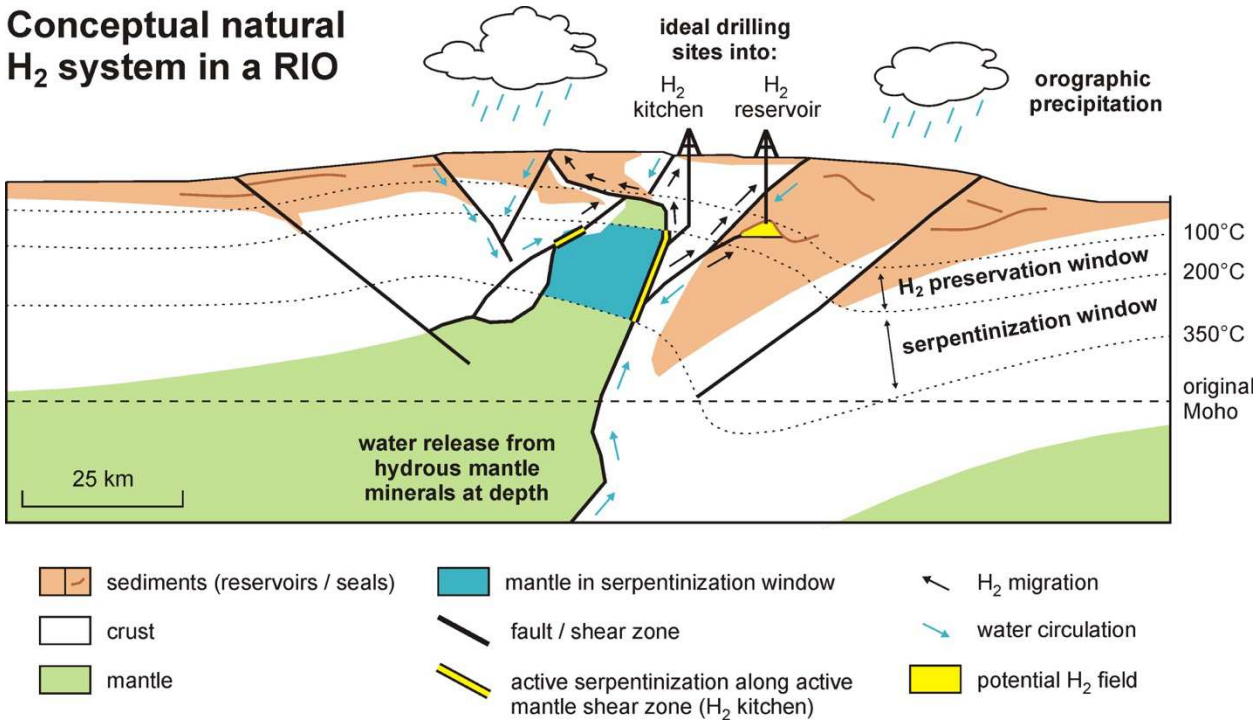

Fig. 6. *Conceptual depiction of a natural H_2 system in a rift-inversion orogen (RIO). Figure based on the geology of panel (2') from Fig. 5. Water, originating from either the deep or the surface, can flow along (active) fault zones towards those parts of the mantle that are in the serpentinization window (200-350˚C), where natural H_2 is being produced ("natural H_2 kitchen"). The natural H_2 can subsequently migrate towards the surface along fault zones, and may accumulate in reservoirs capped by seals of impermeable layers within sedimentary units. Ideally, such natural H_2 accumulation occurs within the 100-200˚C window, in which H_2 is relatively inert (38; 25; 22), so that a conventional natural H_2 field may develop that can be exploited. Alternatively, it would be possible to directly drill into the natural H_2 kitchen.*

REFERENCES CITED

1. Albers, E., Bach, W., Pérez-Gussinyé, M., McCammon, C., and Frederichs, T., 2021, Serpentinization-Driven H2 Production From Continental Break-Up to Mid-Ocean Ridge Spreading: Unexpected High Rates at the West Iberia Margin: Frontiers in Earth Science, v. 9, https://www.frontiersin.org/articles/10.3389/feart.2021.673063

2. Arboleya, M.L., Teixell, A., Charroud, M., Julivert, M., 2004. A structural transect through the High and Middle Atlas of Morocco. Journal of African Earth Sciences, Key Points on African Geology 39, 319–327. https://doi.org/10.1016/j.jafrearsci.2004.07.036

3. Barnes, J., and Sharp, Z., 2006, A chlorine isotope study of DSDP/ODP serpentinized ultramafic rocks: Insights into the serpentinization process: Chemical Geology, v. 228, p. 246–265, https://doi.org/10.1016/j.chemgeo.2005.10.011

4. Cowgill et al., 2016. Relict basin closure and crustal shortening budgets during continental collision: An example from Caucasus sediment provenance, Tectonics. https://doi.org/10.1002/2016TC004295

5. Darin & Umhoefer (2022) Diachronous initiation of Arabia–Eurasia collision from eastern Anatolia to the southeastern Zagros Mountains since middle Eocene time, International Geology Review, 64:18, 2653-2681, https://doi.org/10.1080/00206814.2022.2048272

6. Dugamin, E., Truche, L., Donzé, F.V. 2019. Natural Hydrogen Exploration Guide. https://www.researchgate.net/publication/330728855

7. Emmanuel, S., and Berkowitz, B., 2006, Suppression and stimulation of seafloor hydrothermal convec- tion by exothermic mineral hydration: Earth and Planetary Science Letters, v. 243, p. 657–668, https://doi.org/10.1016/j.epsl.2006.01.028.

8. Erdős, Z., Huismans, R.S., Van der Beek, P., Thieulot, C. (2014). Extensional inheritance and surface processes as controlling factors of mountain belt structure. Journal of Geophysical Research: Solid Earth, 119, 9042-9061. https://doi.org/10.1002/2014JB011408

9. Erdős, Z., Huismans, R.S., and van der Beek, P., 2019, Control of increased sedimentation on orogenic fold-and-thrust belt structure – insights into the evolution of the Western Alps: Solid Earth, v. 10, p. 391–404. https://doi.org/10.5194/se-10-391-2019

10. Faccenna, C. et al., 2014, Mantle dynamics in the Mediterranean: Reviews of Geophysics, v. 52, p. 283–332, https://doi.org/10.1002/2013RG000444

11. Ford, M. et al., 2022, Evolution of a low convergence collisional orogen: a review of Pyrenean orogenesis: Bulletin de la Société Géologique de France, v. 193, p. 19, https://doi.org/10.1051/bsgf/2022018

12. Furnes, H., Dilek, Y., Zhao, G., Safonova, I., Santosh, M., 2020. Geochemical characterization of ophiolites in the Alpine-Himalayan Orogenic Belt: Magmatically and tectonically diverse evolution of the Mesozoic Neotethyan oceanic crust. Earth-Science Reviews 208, 103258. https://doi.org/10.1016/j.earscirev.2020.103258

13. Gaucher, E.C., 2020, New Perspectives in the Industrial Exploration for Native Hydrogen: Elements, v. 16, p. 8–9, https://doi.org/10.2138/gselements.16.1.8

14. Grool, A.R., Huismans, R.S., and Ford, M., 2019, Salt décollement and rift inheritance controls on crustal deformation in orogens: Terra Nova, v. 31, p. 562–568, https://doi.org/10.1111/ter.12428

15. Hänggi, P., Gaucher, E.C., 2023. Exploration of natural hydrogen in the Lower Engadin window, Switzerland. Goldschmidt 2023 Conference, Lyon. https://conf.goldschmidt.info/goldschmidt/2023/meetingapp.cgi/Paper/20741

16. Howarth, R.W., and Jacobson, M.Z., 2021, How green is blue hydrogen? Energy Science & Engineering, v. 9, p. 1676–1687, https://doi.org/10.1002/ese3.956

17. Jammes, S., and Huismans, R.S., 2012, Structural styles of mountain building: Controls of lithospheric rheologic stratification and extensional inheritance: Journal of Geophysical Research: Solid Earth, v. 117, https://doi.org/10.1029/2012JB009376

18. Jammes, S., Huismans, R.S., and Muñoz, J.A., 2014, Lateral variation in structural style of mountain building: controls of rheological and rift inheritance: Terra Nova, v. 26, p. 201–207, https://doi.org/10.1111/ter.12087

19. Jourdon, A., Le Pourhiet, L., Mouthereau, F., and Masini, E., 2019, Role of rift maturity on the architecture and shortening distribution in mountain belts: Earth and Planetary Science Letters, v. 512, p. 89–99. https://doi.org/10.1016/j.epsl.2019.01.057

20. Klein, F., Tarnas, J.D., and Bach, W., 2020, Abiotic sources of molecular hydrogen on Earth: Elements, v. 16, p. 19–24, https://doi.org/10.2138/gselements.16.1.19

21. Lefeuvre, N., Truche, L., Donzé, F.-V., Ducoux, M., Barré, G., Fakoury, R.-A., Calassou, S., and Gaucher, E.C., 2021, Native H2 Exploration in the Western Pyrenean Foothills: Geochemistry, Geophysics, Geosystems, v. 22, p. e2021GC009917, https://doi.org/10.1029/2021GC009917

22. Lefeuvre, N., Truche, L., Donzé, F.-V., Gal, F., Tremosa, J., Fakoury, R.-A., Calassou, S., and Gaucher, E.C., 2022, Natural hydrogen migration along thrust faults in foothill basins: The North Pyrenean Frontal Thrust case study: Applied Geochemistry, v. 145, p. 105396, https://doi.org/10.1016/j.apgeochem.2022.105396

23. Liu, Z., Perez-Gussinye, M., García-Pintado, J., Mezri, L., and Bach, W., 2023, Mantle serpentinization and associated hydrogen flux at North Atlantic magma-poor rifted margins: Geology, https://doi.org/10.1130/G50722.1

24. Mazzoli, S., Algarra, A.M., 2011. Deformation partitioning during transpressional emplacement of a ‘mantle extrusion wedge’: the Ronda peridotites, western Betic Cordillera, Spain. Journal of the Geological Society 168, 373–382. https://doi.org/10.1144/0016-76492010-126

25. McCollom, T.M., 2013. Laboratory Simulations of Abiotic Hydrocarbon Formation in Earth's Deep Subsurface. Reviews in Mineralogy and Geochemistry 75, 467–494. https://doi.org/10.2138/rmg.2013.75.15

26. Mosar, J., Mauvilly, J., Koiava, K., Gamkrelidze, I., Enna, N., Lavrishev, V., Kalberguenova, V., 2022. Tectonics in the Greater Caucasus (Georgia – Russia): From an intracontinental rifted basin to a doubly verging fold-and-thrust belt. Marine and Petroleum Geology 140, 105630. https://doi.org/10.1016/j.marpetgeo.2022.105630

27. Muñoz, J.A., 2019. Alpine Orogeny: Deformation and Structure in the Northern Iberian Margin (Pyrenees s.l.), in: Quesada, C., Oliveira, J.T. (Eds.), The Geology of Iberia: A Geodynamic Approach: Volume 3: The Alpine Cycle, Regional Geology Reviews. Springer International Publishing, Cham, pp. 433–451. https://doi.org/10.1007/978-3-030-11295-0_9

28. Philip, H., Cisternas, A., Gvishiani, A., and Gorshkov, A., 1989, The Caucasus: an actual example of the initial stages of continental collision: Tectonophysics, v. 161, p. 1–21, https://doi.org/10.1016/0040-1951(89)90297-7

29. Robertson, A.H.F., Trivić, B., Đerić, N., Bucur, I.I., 2013. Tectonic development of the Vardar ocean and its margins: Evidence from the Republic of Macedonia and Greek Macedonia. Tectonophysics, The Agean : A natural laboratory for tectonics - Tectonometamorphics 595–596, 25–54. https://doi.org/10.1016/j.tecto.2012.07.022

30. de Saint Blanquat, M., Bajolet, F., Grand'Homme, A., Proietti, A., Zanti, M., Boutin, A., Clerc, C., Lagabrielle, Y., Labaume, P., 2016. Cretaceous mantle exhumation in the

central Pyrenees: New constraints from the peridotites in eastern Ariège (North Pyrenean zone, France). Comptes Rendus Geoscience, From rifting to mountain building: the Pyrenean Belt 348, 268–278. https://doi.org/10.1016/j.crte.2015.12.003

31. Salazar-Mora, C.A., Huismans, R.S., Fossen, H., and Egydio-Silva, M., 2018, The Wilson Cycle and Effects of Tectonic Structural Inheritance on Rifted Passive Margin Formation: Tectonics, v. 37, p. 3085–3101, https://doi.org/10.1029/2018TC004962.

32. Schmid, S.M., Bernoulli, D., Fügenschuh, B., Matenco, L., Schefer, S., Schuster, R., Tischler, M., Ustaszewski, K., 2008. The Alpine-Carpathian-Dinaridic orogenic system: correlation and evolution of tectonic units. Swiss Journal of Geosciences 101, 139–183. https://doi.org/10.1007/s00015-008-1247-3

33. Schmid, S.M., Kissling, E., Diehl, T., van Hinsbergen, D.J.J., Molli, G., 2017. Ivrea mantle wedge, arc of the Western Alps, and kinematic evolution of the Alps–Apennines orogenic system. Swiss Journal of Geosciences 110, 581–612. https://doi.org/10.1007/s00015-016-0237-0

34. Smith, N., 2002, It's time for explorationists to take hydrogen more seriously. First Break. https://doi.org/10.3997/1365-2397.20.4.25031

35. Smith et al. 2005. Hydrogen exploration: a review of global hydrogen accumulations and implications for prospective areas in NW Europe. https://doi.org/10.1144/0060349

36. Tarkowski, R., 2019. Underground hydrogen storage: Characteristics and prospects. Renewable and Sustainable Energy Reviews 105, 86–94. https://doi.org/10.1016/j.rser.2019.01.051

37. Tichadou, C., Godard, M., Muñoz, M., Labaume, P., Vauchez, A., Gaucher, E.C., and Calassou, S., 2021, Mineralogical and geochemical study of serpentinized peridotites from the North-Western Pyrenees: New insights on serpentinization along magma-poor continental passive margins: Lithos, v. 406–407, p. 106521, https://doi.org/10.1016/j.lithos.2021.106521

38. Truche, L., Berger, G., Destrigneville, C., Pages, A., Guillaume, D., Giffaut, E., Jacquot, E., 2009. Experimental reduction of aqueous sulphate by hydrogen under hydrothermal conditions: implication for the nuclear waste storage. Geochem. Cosmochim. Acta 73 (16), 4824–4835. https://doi.org/10.1016/j.gca.2009.05.043.

39. Truche, L., and Bazarkina, E.F., 2019, Natural hydrogen the fuel of the 21st century: E3S Web of Conferences, v. 98, p. 03006, https://doi.org/10.1051/e3sconf/20199803006

40. Vasey, D., Naliboff, J.B., Cowgill, E., Brune, S., Glerum, A., Zwaan, F. (in review). The structural style of intracontinental rift-inversion orogens. Geology. Preprint: https://doi.org/10.31223/X5HM3D

41. Wang, Y., Chevrot, S., Monteiller, V., Komatitsch, D., Mouthereau, F., Manatschal, G., Sylvander, M., Diaz, J., Ruiz, M., Grimaud, F., Benahmed, S., Pauchet, H., Martin, R., 2016. The deep roots of the western Pyrenees revealed by full waveform inversion of teleseismic P waves. Geology 44, 475–478. https://doi.org/10.1130/G37812.1

42. Wilson, R. W., Houseman, G. A., Buiter, S. J. H., McCaffrey, K. J. W., & Doré, A. G. (2019). Fifty years of the Wilson Cycle Concept in Plate Tectonics: An Overview. Geological Society, London, Special Publications, 470, SP470-2019–58. https://doi.org/10.1144/SP470-2019-58

43. Zgonnik, V., 2020, The occurrence and geoscience of natural hydrogen: A comprehensive review: Earth-Science Reviews, v. 203, p. 103140, https://doi.org/10.1016/j.earscirev.2020.103140

44. Zwaan, F., Brune, S., Glerum, A., Vasey, D., Naliboff, J., Manatschal, G., Gaucher, E.C. (2023b): Rift-inversion orogens. https://github.com/geozwaan/rift-inversion_orogens
    a. **NB:** This is part of the Supplement – This GitHub repository will be made into a Zenodo repository with a permanent DOI upon acceptance of the manuscript.

45. Zwaan, F., Brune, S., Glerum, A., Vasey, D., Naliboff, J., Manatschal, G., Gaucher, E.C. (2023b): https://nextcloud.gfz-potsdam.de/s/cYX7yWGtTM7wbBg
    a. **NB:** This is part of the Supplement - The files gathered in this Nextcloud folder will be made into a GFZ data publication with a permanent DOI upon acceptance of the manuscript.

[1]Supplemental Material.

Modelling software, input files, and details on model analysis methods are publicly available here: https://github.com/geozwaan/rift-inversion_orogens (44). Moreover, a GFZ data publication

containing supplementary material (additional details on model results, as well as videos of each model) is publicly available here: https://nextcloud.gfz-potsdam.de/s/cYX7yWGtTM7wbBg (45).

ONLINE METHODS

I. Numerical method

We base our modelling approach on previous work by Neuharth et al. (2022) (61), using the thermo-mechanical geodynamic code ASPECT (Advanced Solver for Problems in Earth's ConvecTion) (58; 55; 63; 53; 54; 47; 48), coupled with FastScape (50; 69, 70; 61) for the inclusion of surface processes (Fig. M1). We apply a modified version of ASPECT 2.4.0-pre for the coupling with Fastscape. ASPECT and FastScape installation details, the custom ASPECT plugins we use, the parameter files used for each model run, the log files of each model run, and the Paraview state files used for model analysis are provided in a publicly accessible GitHub repository (44) (https://github.com/geozwaan/rift-inversion_orogens) that will be archived with a DOI at Zenodo as soon as the manuscript is accepted for the publication.

Geodynamic modelling (ASPECT)

We apply ASPECT to solve the conversation equation under the extended Boussinesq approximation.

Conservation of momentum is described in the following equation:

$$-\nabla \cdot 2\eta\dot{\varepsilon}(u) + \nabla P = \rho g \qquad \text{(eq. M1)},$$

where η is viscosity, $\dot{\varepsilon}$ is the deviatoric strain rate, u is velocity, P is pressure, ρ is density, and g is gravitational acceleration.

Conservation of mass is described as follows:

$$\nabla \cdot u = 0 \qquad \text{(eq. M2)},$$

548 Conservation of energy defined as:

549 $$\bar{\rho} C_p \left(\frac{\partial T}{\partial t} + u \cdot \nabla T\right) - \nabla \cdot k \nabla T = \bar{\rho} H + (2\eta \dot{\varepsilon}) : \dot{\varepsilon} - \alpha \rho T (u \cdot g) \quad \text{(eq. M3)},$$

550 where $\bar{\rho}$ is the reference adiabatic density, C_p the specific heat capacity, T the temperature, k the
551 thermal conductivity, H the radiogenic heating, and α the thermal expansivity. The right-hand
552 terms represent radioactive heating, viscous shear heating, and adiabatic heating, respectively. Sea
553 Table M1 for the used parameter values.

554

555 Each compositional field c_i (e.g., representing lithologies such as the upper crust, or strain fields)
556 is advected with the calculated velocity field:

557 $$\frac{\partial c_i}{\partial t} + u \cdot \nabla c_i = q_i \qquad \text{(eq. M3)},$$

558 where reaction rate q_i is non-zero for the plastic (brittle) and viscous strain fields.

559

560 *Landscape modelling (FastScape)*

561 FastScape modifies ASPECT's model domain's surface as a function of stream-power law fluvial
562 erosion, hillslope and marine diffusion, horizontal advection and vertical uplift (where in the latter
563 two cases, the X and Y velocities and the Z velocities from ASPECT are used as model input) (50;
564 69; 70). Topograhy changes in the continental domain ($h \geq h_{sea}$) are therefore described by the
565 following equation:

566 $$\frac{dh}{dt} = U - K_f A^m S^n + \frac{G}{A} \int_A \left(U - \frac{dh}{dt}\right) dA + K_c \nabla^2 h + v \cdot \nabla h \qquad \text{(eq. M4)},$$

567 Where h is the topographic elevation, U the uplift rate, K_f the bedrock erodibility, A the drainage
568 area, S the slope, m the drainage area exponent, n the slope exponent, G the deposition coefficient,
569 K_c the continental diffusion coefficient, and v the horizontal velocity. See Table M2 for the used
570 parameter values.

571

572 Moreover, marine processes ($h < h_{sea}$) are described as follows:

573 $$\frac{dh}{dt} = K_m \nabla^2 h + Q_s + v \cdot \nabla h + Q_o \qquad \text{(eq. M5)},$$

574 where K_m represents the marine diffusion coefficient, Q_s the sediment flux from the continent to
575 the marine domain at the continent-marine boundary (70), and Q_o a homogeneous marine
576 background sedimentation rate.

577
578

579 **II. Geodynamic Model design**

580 *Model geometry*

581 Our 2D rectangular domain is 450 km long and 200 km high and contains three layers together
582 representing a 115 km thick stable continental lithosphere: (I) a 20 km thick wet quartzite upper
583 crust (64), (II) a 15 km thick wet anorthite lower crust (65), and (III) an 80 km thick lithospheric
584 mantle consisting of dry olivine (46; 62), overlying a wet olivine asthenosphere (56) (Fig. M1a,
585 Table M1). Thicker upper crust (25 km) in the model domain centre (between x = 150 km and x =
586 300 km, following a Gaussian distribution) produces a weaker strength profile and localizes
587 kinematically-driven tectonic deformation in this region (Fig. M1b). Furthermore, a randomized
588 initial plastic (brittle) strain pattern with a maximum value of 0.5 is introduced in the upper 50 km
589 of the crust to assist strain localization (Fig. M1a). The initial temperature follows a 1D steady-
590 state continental geotherm in the lithosphere (51) and an adiabatic profile below.

591

592 *Viscoplastic rheology and weakening processes*

593 We use a visco-plastic rheology (59) that combines diffusion creep, dislocation creep and Drucker-
594 Prager plasticity. The friction angle is linearly weakened up to 4 times between brittle strain values
595 of 0 and 1 (Fig. M1c, Table M1). Similarly, we apply a 4 times pre-yield viscous weakening

between these same values of the viscous strain. Picard iterations on the Stokes solution are used to solve up to a nonlinear tolerance of $2 \cdot 10^{-5}$ for a maximum of 120 iterations per time step.

Boundary conditions

A fixed temperature of 0˚C is prescribed at the surface, and a temperature of 1361˚C at the bottom boundary. Tectonic deformation (divergence and convergence) is induced by prescribing outward and inward flow on the lateral model boundaries, respectively (Fig. M1a). This prescribed horizontal boundary velocity is 5 mm y^{-1} on either lateral boundary, making for a total velocity of 10 mm/yr during either rifting or inversion. Flow through the lateral boundaries is compensated by inflow and outflow through the bottom boundary, which is controlled by a traction boundary condition set to a lithostatic pressure of $6.1 \cdot 10^{9}$ Pa (Fig. M1a). The latter boundary condition is imposed to conserve mass within the ASPECT model over time and to ensure isostatically balanced topography. Tectonic quiescence (leading to post-rift cooling) between divergence and convergence phases is simulated by prescribing a velocity of zero at the lateral model boundaries.

FastScape parameters

We adopt a sea-level of 500 m below the initial surface level of the ASPECT model domain, a value that corresponds to the average elevation of stable continents with ~35 km crust far away from hotspots (66). All FastScape parameters are specified in Table M2. In particular, we apply a fluvial erosion coefficient (K_f) of 10^{-5} $m^{0.2}$ yr^{-1} and a continental hillslope diffusivity coefficient (K_c) of $5 \cdot 10^{-3}$ m^2 yr^{-1} that are in agreement with previous model and observational constraints (see Yuan et al. 2019a [69], and references therein).

Numerical aspects

The ASPECT mesh cell size is 10 km at the bottom of the domain, with a three-step refinement down to 1250 m above the 750˚C isotherm, in order to properly capture brittle deformation in the colder parts of the lithosphere. We use second-order (Q2Q1) elements, and to optimally visualize the solution, results are output and analysed on a grid with double the resolution of each cell (Fig. M1), the maximum resolution being 625 m.

III. Varied model parameters

We systematically test the impact of plate tectonic parameters in our rift-inversion orogen models (Table M3). First, we apply different initial rifting durations of 5, 15 and 25 Myr, at a total plate motion velocity of 10 mm yr^{-1}. These values roughly reflect the varying degrees of rifting prior to convergence in (e.g., the High Atlas, Pyrenees, and Alps) (e.g., 49; 11; 60), whereas reference total convergence duration in all these models (30 Myr at a velocity of 10 mm yr^{-1}) reflects the duration of collision in the Pyrenees (11). Second, we vary the duration of the post-rift tectonic quiescence period from 0 to 20 to 40 Myr, which also reflect values seen in natural rift-inversion orogens (49; 11; 60).

IV. Model analysis

We extract for each model the following three metrics over time: (I) the area of exhumed mantle, i.e. total area of mantle above the initial Moho at 35 km depth, Figs. 2, M1), (II) the area of actively rising exhumed mantle (i.e. the area of exhumed mantle with upward vertical velocity > 0 m s^{-1}), (III) the serpentinization window (i.e. the area of mantle within the 200-350˚C temperature window in which serpentinization is most efficient) (7). This quantification step is performed using the open source Paraview visualisation software (www.paraview.org).

We furthermore adopt the general approach of Liu et al. (2023) (23) to calculate serpentinization capacity in kg(km yr)$^{-1}$ and associated H_2 generation potential in mol(km yr)$^{-}$1 in geodynamic models. This approach is based on the assumption that active and sufficiently mature faults feature a high permeability, which allows for sufficient water circulation to enable high-degree serpentinization of mantle rocks. Therefore, at each output time step, we quantify the area of mantle rocks that have accumulated a total plastic (i.e., brittle) strain $\varepsilon \geq 0.5$ and that undergo significant active deformation (second strain rate invariant $[\dot{\varepsilon}] \geq 2.5 \cdot 10^{-15}$). Note that we also test different strain and strain rate thresholds to estimate the variability in the results of our analysis (see Supplementary Material) (45). We find that reasonably different thresholds do not change our conclusions.

Using the area of actively deforming mantle rocks, we subsequently adopt the temperature-dependent serpentinization reaction formulas from Emmanuel & Berkowitz (2006) and Liu et al. (2023) (7, 23) to compute serpentinization rates using Paraview's Python calculator application:

$$\frac{\partial Dserp}{\partial t} = Ae^{(-b_s(T-c_s)^2} \qquad \text{(Eq. 6)},$$

where $\frac{\partial Dserp}{\partial t}$ is the serpentinization rate of a given element (unit: s^{-1}), and T is the temperature in degrees Celsius, while empirically fitted kinetic coefficients ($A = 10^{-10}$ s^{-1}, $b_s = 2.5 \times 10^{-4}$ $C^{\circ-2}$, c_s = 270˚C), have been derived from experimental and theoretical observations on serpentinization kinematics (7).

With the serpentinization rate, we can calculate the serpentinization capacity (M_t) along the modelled section using the following equation from Liu et al. (2023) (23) in the Paraview Python calculator:

$$M_t = \sum_{i=1}^{i=nel} \left(\frac{\partial Dserp}{\partial t}\right)(i)\, S_i\, \rho_m \qquad \text{(Eq. 7)}$$

where $\left(\frac{\partial Dserp}{\partial t}\right)(i)$ is the serpentinization rate of a given element I, with S_i being the area of that element, and ρ_m the density of the material in that element. By summing over all elements (*nel*), and given that our geodynamic ASPECT model is 2D, we obtain M_t in units of kg(m s)$^{-1}$, which we convert to kg(km yr)$^{-1}$. Here the km indicates length along-strike of the tectonic system (i.e. perpendicular to the 2D geodynamic ASPECT model, Figs. 2, M1).

The serpentinization capacity value enables us to calculate the cumulative mass of serpentinized mantle in units of kg km^{-1} perpendicular to the model for each model data output interval of 500 kyr. We subsequently calculate the natural H_2 capacity in units of mol(km yr)$^{-1}$, as well as the

686 cumulative natural H_2 generation in units of mol km^{-1}. We assume that 1 kg of serpentinized mantle
687 material generates 300 mmol of natural H2, which is an upper limit reported by Albers et al. (2021)
688 (1), and the resulting values thus represent an upper limit estimate of the natural H_2 capacity and
689 cumulative natural H_2 generation in our models.
690
691 **V. Nuances to our model analysis**
692 We must consider some nuances to our model approach. Our models are essentially 2D (Fig. 2),
693 whereas natural orogens are complex 3D structures (e.g., 60), each with a unique history that
694 requires assessment of H_2 potential on a case-by-case basis (39). This assessment concerns their
695 tectonic history, but also the type (composition) of mantle material and the origin and associated
696 chemistry of the water involved in serpentinization, which modulates natural H_2 generation
697 potential (1; 59; 37). Other limitations to our models concern the omission of detailed sedimentary
698 history (i.e., timing and availability of reservoirs and seals), as well as detailed natural H_2 migration
699 pathways to these reservoirs (e.g., 21; 22). In this context, the impact of density changes during
700 serpentinization also requires attention, since the volumetric expansion of serpentinizing mantle
701 material may either clog water and hydrogen pathways (52) or induce new fracturing and increase
702 permeability (67). Finally, H_2 gas is highly reactive and may easily be consumed by (bio)chemical
703 reactions on its way to, or within reservoirs (e.g., 57; 68). Still, our model results provide a solid,
704 first-order impression of the natural H_2 potential of rift-inversion orogens.
705

FIGURES – METHODS

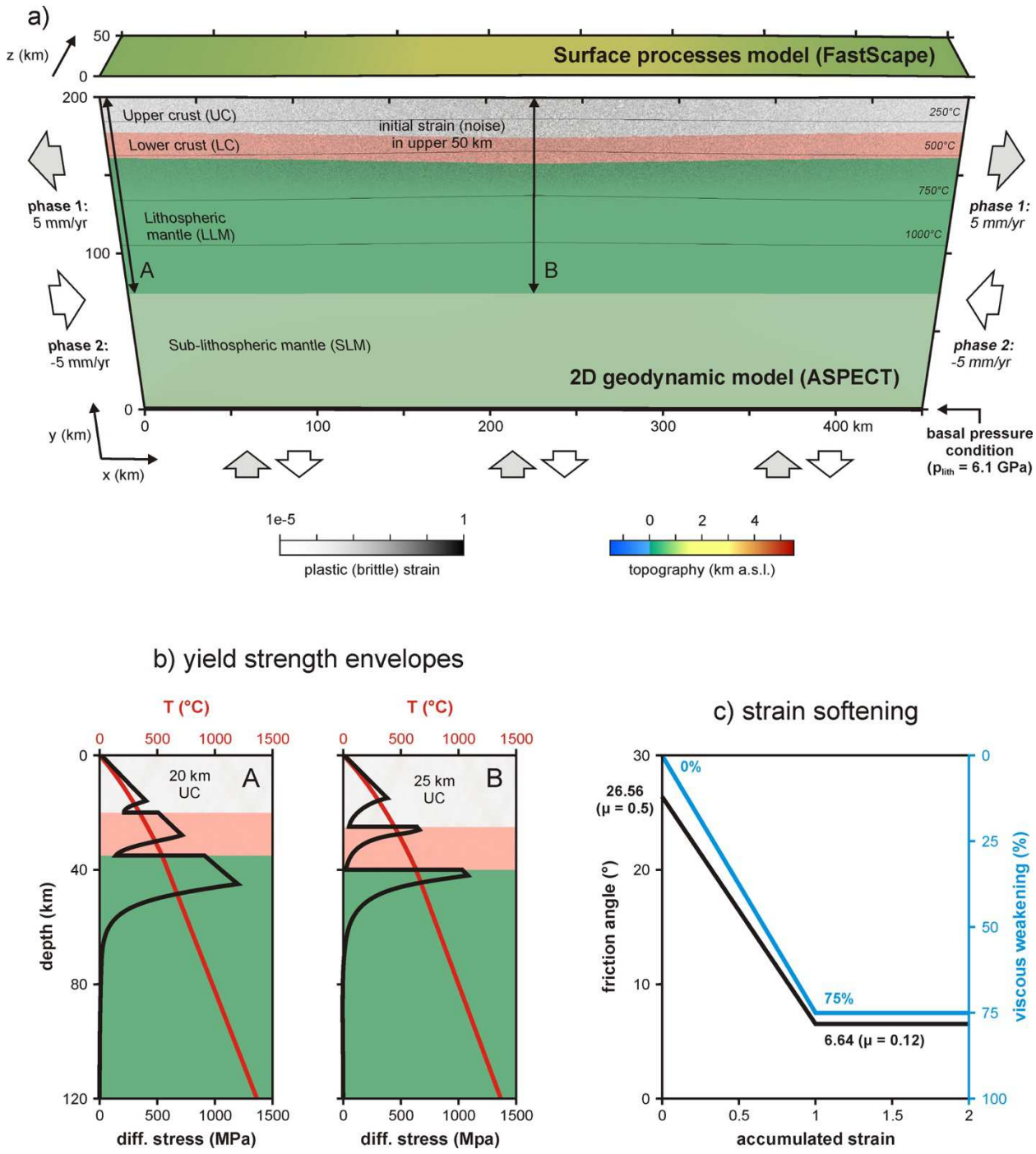

Methods Figure M1. *Reference model set-up. (a) 3D Visualization of the 2D geodynamic model (ASPECT) with the quasi-3D surface processes model (FastScape) on top. Black lines indicate temperature contours and initial strain (noise) at t = 0 Myr is present in the uppermost 50 km. (A) and (B) indicate the outer and central locations of the yield strength profiles depicted in panel (b), which have different crustal thicknesses as the upper crust in the model centre is 25 km instead of 20 km thick. (b) Yield strength and temperature profiles along (A) and (B) shown in panel (a). (c) Plastic (brittle) and viscous weakening intervals applied in our models. Modified after Neuharth et al. (2022) (61).*

Methods table M1 – Basic ASPECT parameters

Parameter	Symbol	Units	Sediment	Upper crust	Lower crust	Lithospheric mantle	Sub-lithospheric mantle
Reference surface density*	ρ_0	kg m^{-3}	2520	2700	2850	3280	3300
Adiabatic surface temperature	T_{AS}	˚C	1284	1284	1284	1284	1284
LAB isotherm temperature	T_{LAB}	˚C	1284	1284	1284	1284	1284
Thermal expansivity	α	K^{-1}	$3.7\cdot10^{-5}$	$2.7\cdot10^{-5}$	$2.7\cdot10^{-5}$	$3.0\cdot10^{-5}$	$3.0\cdot10^{-5}$
Thermal diffusivity	κ	m^2 s^{-1}	$7.28\cdot10^{-7}$	$7.72\cdot10^{-7}$	$7.31\cdot10^{-7}$	$8.38\cdot10^{-7}$	$8.33\cdot10^{-7}$
Heat capacity	C_p	J kg^{-1} K^{-1}	1200	1200	1200	1200	1200
Heat production	H	W m^{-3}	$1.2\cdot10^{-6}$	$1.0\cdot10^{-6}$	$0.1\cdot10^{-6}$	0	0
Cohesion	C	Pa	$5\cdot10^{6}$	$5\cdot10^{6}$	$5\cdot10^{6}$	$5\cdot10^{6}$	$5\cdot10^{6}$
Internal friction angle (unweakened)	ϕ	◦	26.56	26.56	26.56	26.56	26.56
Plastic strain weakening interval	-	-	[0,1]	[0,1]	[0,1]	[0,1]	[0,1]
Plastic strain weakening factor	ϕ_{wf}	-	0.25	0.25	0.25	0.25	0.25
Viscous strain weakening interval	-	-	[0,1]	[0,1]	[0,1]	[0,1]	[0,1]
Viscous strain weakening factor	-	-	0.25	0.25	0.25	0.25	1.0
*Creep properties***			*Wet quartzite*	*Wet quartzite*	*Wet anorthite*	*Dry olivine*	*Wet olivine*
Stress exponent (dis)	n	-	4.0	4.0	3.0	3.5	3.5
Constant prefactor (dis)	A_{dis}	Pa^{-n}s^{-1}	$8.57\cdot10^{-28}$	$8.57\cdot10^{-28}$	$7.13\cdot10^{-18}$	$6.52\cdot10^{-16}$	$2.12\cdot10^{-15}$
Activation energy (dis)	E_{dis}	J mol^{-1}	$223\cdot10^{3}$	$223\cdot10^{3}$	$345\cdot10^{3}$	$530\cdot10^{3}$	$480\cdot10^{3}$
Activation volume (dis)	V_{dis}	m^3 mol^{-1}	0	0	$38\cdot10^{-6}$	$18\cdot10^{-6}$	$11\cdot10^{-6}$
Constant prefactor (diff)	A_{diff}	Pa^{-1}s^{-1}	$5.79\cdot10^{-19}$	$5.79\cdot10^{-19}$	$2.99\cdot10^{-25}$	$2.25\cdot10^{-9}$	$1.5\cdot10^{-9}$
Activation energy (diff)	E_{diff}	J mol^{-1}	$223\cdot10^{3}$	$223\cdot10^{3}$	$159\cdot10^{3}$	$375\cdot10^{3}$	$335\cdot10^{3}$
Activation volume (diff)	V_{diff}	m^3 mol^{-1}	0	0	$38\cdot10^{-6}$	$6\cdot10^{-6}$	$4\cdot10^{-6}$
Grain size (diff)	d	m	0.001	0.001	0.001	0.001	0.001
Grain size exponent (diff)	m	-	2.0	2.0	3.0	0	0

* Model input densities are scaled so that at surface temperatures (T_0 = 273˚ K or 0˚C) these values are reached.
** Creep properties: dis = dislocation creep, diff = diffusion creep.

Methods table M2 – Basic Fastscape parameters

Parameter	Symbol	Unit	Value
Drainage area exponent	m	-	0.4
Slope exponent	n	-	1
Bedrock/sediment diffusivity	K_c	m^2 yr^{-1}	$5\cdot10^{-3}$
Bedrock/sediment erodibility	K_f	m$^{0.2}$ yr^{-1}	$1\cdot10^{-5}$
Bedrock/sediment deposition coefficient	G	-	1
Marine diffusivity	K_m	m^2 yr^{-1}	200
Sand/shale ratio	F	-	1
Sand/shale porosity	φ	-	0
Sand/shale e-folding depth	z	m	0
Depth averaging thickness	L	m	100
Background sedimentation rate	-	m yr^{-1}	0

Methods table M3 – Variable model parameters

Model name	Rifting duration	Post-rift cooling duration
M1*	5 Myr	0 Myr
M2	15 Myr	0 Myr
M3	25 Myr	0 Myr
M4	5 Myr	20 Myr
M5*	15 Myr	20 Myr
M6	25 Myr	20 Myr
M7	5 Myr	40 Myr
M8	15 Myr	40 Myr
M9*	25 Myr	40 Myr

* End-member models shown in Figs. 3-5

ADDITIONAL REFERENCES CITED IN METHODS SECTION

46. Artemieva, I. M. (2006). Global 1° × 1° thermal model TC1 for the continental lithosphere: Implications for lithosphere secular evolution. Tectonophysics, 416, 245–277. https://doi.org/10.1016/j.tecto.2005.11.022

47. Bangerth, W., Dannberg, J., Fraters, M. Gassmoeller, R., Glerum, A., Heister, T., Myhill, R., Naliboff, J. (2023). Geodynamics/Aspect: ASPECT 2.5.0 (version v2.5.0). Zenodo. https://doi.org/10.5281/ZENODO.8200213

48. Bangerth, W., Dannberg, J., Fraters, M. Gassmoeller, R., Glerum, A., Heister, T., Myhill, R., Naliboff, J. (2023). "ASPECT: Advanced Solver for Problems in Earth's ConvecTion, User Manual." Figshare. https://doi.org/10.6084/M9.FIGSHARE.4865333.

49. Beauchamps, W., Allmendinger, R.W., Barazangi, M., Demnati, A., El Alji, Ml., and Dahmani, M. (1999). Inversion tectonics and the evolution of the High Atlas Mountains, Morocco, based on a geological-geophysical transect. Tectonics, 18, 163-184. https://doi.org/10.1029/1998TC900015

50. Braun, J., & Willett, S. D. (2013). A very efficient O(n), implicit and parallel method to solve the stream power equation governing fluvial incision and landscape evolution. Geomorphology, 180–181, 170–179. https://doi.org/10.1016/J.GEOMORPH.2012.10.008

51. Chapman, D.S., 1986, Thermal gradients in the continental crust: Geological Society, London, Special Publications, v. 24, p. 63–70, https://doi.org/10.1144/GSL.SP.1986.024.01.07.

52. Farough, A., Moore, D.E., Lockner, D.A., Lowell, R.P., 2016. Evolution of fracture permeability of ultramafic rocks undergoing serpentinization at hydrothermal conditions: An experimental study. Geochemistry, Geophysics, Geosystems 17, 44–55. https://doi.org/10.1002/2015GC005973

53. Gassmöller, R., Lokavarapu, H., Heien, E., Puckett, E. G., and Bangerth, W., 2018, Flexible and Scalable Particle-in-Cell Methods With Adaptive Mesh Refinement for Geodynamic Computations. Geochemistry, Geophysics, Geosystems 19, 3596–3604, https://doi.org/10.1029/2018GC007508

54. Glerum, A., Thieulot, C., Fraters, M., Blom, C., and Spakman, W., 2018, Nonlinear viscoplasticity in viscoplasticity in ASPECT: benchmarking and applications to subduction. Solid Earth 9, 267–294, https://doi.org/10.5194/se-9-267-2018

55. Heister, T., Dannberg, J., Gassmöller, R., & Bangerth, W. (2017). High accuracy mantle convection simulation through modern numerical meth- ods—II: Realistic models and problems. Geophysical Journal International, 210, 833–851. https://doi.org/10.1093/gji/ggx195

56. Hirth, G., & Kohlstedt, D. (2003). Rheology of the upper mantle and the mantle wedge: A view from the experimentalists: Inside the subudction factory geophysical monograph (p. 183). American Geophysical Union. https://doi.org/10.1029/138GM06

57. Klein et al. 2015, Fluid mixing and the deep biosphere of a fossil Lost City-type hydrothermal system at the Iberia Margin. PNAS 112, 12036-12041 https://doi.org/10.1073/pnas.1504674112

58. Kronbichler, M., Heister, T. & Bangerth, W., 2012, High accuracy mantle convection simulation through modern numerical methods. Geophysical Journal International 191, 12–29, https://doi.org/10.1111/j.1365-246X.2012.05609.x

59. Lamadrid, H.M., Rimstidt, J.D., Schwarzenbach, E.M., Klein, F., Ulrich, S., Dolocan, A., Bodnar, R.J., 2017. Effect of water activity on rates of serpentinization of olivine. Nat Commun 8, 16107. https://doi.org/10.1038/ncomms16107

60. Manatschal, G., Chenin, G., Lescoutre, R., Miró, J., Cadenas, P., Saspiturry, N., Masini, E., Chevrot, S., Ford, M., Jolivet, L., Mouthereau, F., Thinon, I., Issautier, B., Calassou., S. (2021). The role of inheritance in forming rifts and rifted margins and building collisional orogens: a Biscay-Pyrenean perspective: Bulletin de la Société Géologique de France, v. 192, p. 55. https://doi.org/10.1051/bsgf/2021042

61. Neuharth, D., Brune, S., Wrona, T., Glerum, A., Braun, J., and Yuan, X., 2022, Evolution of Rift Systems and Their Fault Networks in Response to Surface Processes: Tectonics, v. 41, p. e2021TC007166, https://doi.org/10.1029/2021TC007166.

62. Pasyanos, M. E., Masters, T. G., Laske, G., & Ma, Z. (2014). LITH1.0: An updated crust and lithospheric model of the Earth. Journal of Geophysical Research: Solid Earth, 119, 2153–2173. https://doi.org/10.1002/2013jb010626

63. Rose, I., Buffett, B., & Heister, T. (2017). Stability and accuracy of free surface time integration in viscous flows. Physics of the Earth and Plan- etary Interiors, 262, 90–100. https://doi.org/10.1016/j.pepi.2016.11.007

64. Rutter, E. H., & Brodie, K. H. (2004). Experimental grain size-sensitive flow of hot-pressed Brazilian quartz aggregates. Journal of Structural Geology, 26, 2011–2023. https://doi.org/10.1016/j.jsg.2004.04.006

65. Rybacki, E., Gottschalk, M., Wirth, R., & Dresen, G. (2006). Influence of water fugacity and activation volume on the flow properties of fine- grained anorthite aggregates. Journal of Geophysical Research, 111. https://doi.org/10.1029/2005JB003663

66. Theunissen, T., Huismans, R. S., Lu, G., & Riel, N. (2022). Relative continent - mid-ocean ridge elevation: A reference case for isostasy in geodynamics. Earth-Science Reviews, 233, 104153. https://doi.org/10.1016/j.earscirev.2022.104153

67. Uno, M., Koyanagawa, K., Kasahara, H., Okamoto, A., Tsuchiya, N., 2022. Volatile-consuming reactions fracture rocks and self-accelerate fluid flow in the lithosphere. Proceedings of the National Academy of Sciences 119, e2110776118. https://doi.org/10.1073/pnas.2110776118

68. Worman, S.L., Pratson, L.F., Karson, J.A., and Schlesinger, W.H., 2020, Abiotic hydrogen (H2) sources and sinks near the mid-ocean ridge (MOR) with implications for the subseafloor bio- sphere: Proceedings of the National Academy of Sciences of the United States of America, v. 117, p. 13,283–13,293, https://doi.org/10.1073/pnas .2002619117.

69. Yuan, X. P., Braun, J., Guerit, L., Rouby, D., & Cordonnier, G. (2019). A new efficient method to solve the stream power law model taking into account sediment deposition. Journal of Geophysical Research: Earth Surface, 124, 1346–1365. https://doi.org/10.1029/2018JF004867

70. Yuan, X. P., Braun, J., Guerit, L., Simon, B., Bovy, B., Rouby, D., et al. (2019). Linking continental erosion to marine sediment transport and deposition: A new implicit and O(N) method for inverse analysis. Earth and Planetary Science Letters, 524, 115728. https://doi.org/10.1016/j. epsl.2019.115728